

Evaluating Adversarial Robustness in the Spatial Frequency Domain

Keng-Hsin Liao, Chin-Yuan Yeh, Hsi-Wen Chen, Ming-Syan Chen
National Taiwan University
cyyeh@arbor.ee.ntu.edu.tw

Abstract

Convolutional Neural Networks (CNNs) have dominated the majority of computer vision tasks. However, CNNs' vulnerability to adversarial attacks has raised concerns about deploying these models to safety-critical applications. In contrast, the Human Visual System (HVS), which utilizes spatial frequency channels to process visual signals, is immune to adversarial attacks. As such, this paper presents an empirical study exploring the vulnerability of CNN models in the frequency domain. Specifically, we utilize the discrete cosine transform (DCT) to construct the Spatial-Frequency (SF) layer to produce a block-wise frequency spectrum of an input image and formulate Spatial Frequency CNNs (SF-CNNs) by replacing the initial feature extraction layers of widely-used CNN backbones with the SF layer. Through extensive experiments, we observe that SF-CNN models are more robust than their CNN counterparts under both white-box and black-box attacks. To further explain the robustness of SF-CNNs, we compare the SF layer with a trainable convolutional layer with identical kernel sizes using two mixing strategies to show that the lower frequency components contribute the most to the adversarial robustness of SF-CNNs. We believe our observations can guide the future design of robust CNN models.

1. Introduction

Convolutional neural networks (CNNs) have excelled at computer vision tasks, including image classification [16], object detection [37], and image segmentation [29]. However, it has been demonstrated that these models are vulnerable to adversarial attacks, which apply imperceptible perturbations on input images to *fool* targeted CNN models, *e.g.*, to cause wrong classification results. This raises concerns about whether current CNN models should be deployed on safety-critical applications [13]. One approach is to try to improve robustness by training CNN models with their adversarial examples, which is known as adversarial training [30, 2, 46, 53, 54]. Nevertheless, CNN models still could not function reliably when facing adversarial attacks.

Croce *et al.* [5] show that state-of-the-art defense strategies could not surpass 60% accuracy on the ImageNet dataset. Other disadvantages of adversarial training includes a reduction in accuracy on natural unaltered inputs [43, 30] and a significant increase in training cost [40].

As an alternative route, researchers have focused on developing more robust architectures to defend against adversarial attacks [50, 6]. Because humans are not fooled by (and may not even notice) adversarial examples, several studies have been conducted to investigate the Human Visual System (HVS) to find possible mechanisms that can improve adversarial robustness. Vuyyuru *et al.* [50], for example, mimic human eye fixations with a non-uniform sampling of multiple receptive fields at different sizes and locations to strengthen the robustness of CNNs. Dapello *et al.* [6] design convolutional layers to simulate a primary visual cortex to obtain better robustness.

Yet, a fundamental understanding that the HVS utilizes spatial frequency information is absent in the above works. According to the spatial frequency theory [8, 32], the HVS uses spatial frequency channels and is more sensitive to low-frequency changes than high-frequency changes [49, 31, 38].¹ In contrast, recent efforts have demonstrated that CNN models may overly rely on human-imperceptible high-frequency patterns for downstream tasks [52, 11], which also explains CNN's vulnerability towards adversarial examples [22, 52]. On the other hand, several works deploy CNN models in the frequency domain [15, 10, 55], which we denote as *Spatial Frequency CNN (SF-CNN)*. Nevertheless, their works focus on task performance [35] and computation efficiency [55] by leveraging the widely used JPEG standard [51]. In contrast, the disparity between the HVS and the CNN designs prompts us to explore the potential impact of spatial frequency features on adversarial vulnerability.

We address these questions by presenting an empirical evaluation of the SF-CNN models compared with the normal CNN models. Specifically, we employ well-known CNN model structures (*i.e.*, ResNet [16], EfficientNet [45],

¹Spatial frequencies denote the periodic spectrum of visual signals across the image input, which can entail rich semantic information [55].

and DenseNet [19]), but replace the first few convolutional layers with *Spatial Frequency (SF)* layer, which retrieves a block-wise spatial frequency spectrum. By these models, we compare the adversarial robustness of a convolution-based feature extractor (the first few CNN layers) with a spatial frequency feature extractor.² Our experiments demonstrate that SF-CNNs outperform standard CNNs in terms of model robustness under both white-box and black-box attacks. For all evaluated datasets, SF-CNNs achieve *higher* accuracy than CNN models with similar architectures under the standard white-box attack, (*i.e.*, the Projected Gradient Descent attack [30]). Furthermore, SF-CNNs are much more robust than CNNs when facing adversarial examples generated from other CNN and SF-CNN models (*i.e.*, transfer attacks [34]). Finally, we compare the SF layer to a trainable convolutional layer and find that SF-CNN models utilize low-frequency channels better than CNN models. In addition, with two mixing strategies, *i.e.*, *interpolation* and *substitution*, we observe that the kernel weights of the first feature extraction layer contribute significantly to the robustness of a model.

The following is a summary of contributions.

- To the best of our knowledge, this is the first work that provides a thorough evaluation of the adversarial robustness of SF-CNNs.
- This paper investigates the performance of SF-CNNs under white-box and black-box attacks empirically. The experimental results show that using spatial frequency channels as a feature extractor, SF-CNNs outperform standard CNN models under all types of attacks.
- To further investigate the SF layer, we propose two mixing strategies between SF-CNNs and standard CNNs. The results show that the use of lower frequency components is related to the robustness of SF-CNNs.

2. Related works

2.1. Adversarial attack and defense

The objective of an adversarial attack is to create adversarial examples that deceive the targeted model by introducing human-imperceptible perturbations to natural images [44]. Based on the attacker’s capabilities, adversarial attacks can be categorized into white-box or black-box attacks. Under the white-box setting, attackers have direct

²In practice, we divide the input images into 8×8 pixel blocks, then utilize the Discrete Cosine Transform (DCT) [1] to extract horizontal and vertical spatial frequency components within each block. Our spatial frequency extraction process closely resembles the widely used JPEG compression standard [51], which was also inspired by the use of spatial frequencies in the HVS.

access to the model weights and may perform gradient calculations [14, 30] or other optimization techniques [44, 3] to effectively obtain the precise adversarial patterns. As a standard first-order attack for evaluation of adversarial robustness [56, 50], the Projected Gradient Descent (PGD) attack [30] generates adversarial examples using an iterative gradient descent operation. Under the black-box setting, the attackers may employ the aforementioned gradient schemes by querying the target model to estimate the gradient via zero-order optimizations [48]. Otherwise, they may construct *surrogate models* to conduct *transfer attacks*, in which adversarial examples generated from a surrogate model are applied to the targeted model. The empirical evidence for standard CNNs’ vulnerability to transfer attacks is well documented [34, 28]. Demontis *et al.* [7] show, in particular, that the complexity of the surrogate model and the target model influences the transferability of adversarial examples. Inkawhich *et al.* [23] demonstrate that directly perturbing in the feature space of the hidden layers yields adversarial examples that are highly transferable.

To defend against adversarial attacks, many researchers propose different adversarial training strategies that retrain the target model on its adversarial examples to achieve better robustness [14, 30]. Nonetheless, the approach is unsatisfactory due to the high computation cost [47] and the trade-off between standard accuracy and robustness [56]. Thus, some researchers have also sought alternative mechanisms that may help bring the models closer to human-level robustness [50]. For instance, Kang *et al.* [24] leverage neural Ordinary Differential Equations to maintain a stable model response towards adversarial perturbations. Dong *et al.* [9] achieve robustness with AdderNets, which replaces the multiplications in a convolutional layer with additions. However, the aforementioned works require substantial modifications to the standard CNN design. In contrast, we investigate the possibility of achieving adversarial robustness simply by utilizing the spatial frequencies as the initial feature for CNN models.

2.2. Learning in the frequency domain

Since condensed signals in the spatial frequency domain provide much information for computer vision tasks, several recent works incorporate the spatial frequency extraction process in CNNs for task performance [55, 35], computation efficiency [15, 10], or model compression [27, 4]. Gueguen *et al.* [15] and Ehrlich *et al.* [10] modify the CNN models to encode the compressed JPEG code [51] for a faster operation speed. In addition, Qin *et al.* [35] include an attention module on the frequency channels to improve image classification accuracy. Motivated by these initial attempts, subsequent research extended frequency learning to a variety of tasks, including domain generalization [20], adaptation [21], and instance segmentation [41]. Further-

more, the frequency spectrum has also been used to investigate standard CNNs. Wang *et al.* [52] argue that CNNs rely on high-frequency components since CNNs achieve higher accuracy on high-frequency reconstructions of test images. They also empirically showed that smoothing the kernel weights can often provide adversarial robustness despite causing substantial reductions in task accuracy as well. Nevertheless, with these advancements, the adversarial robustness of CNN models trained in the spatial frequency domain has not been assessed.

3. Methodology

In this study, we examine the adversarial robustness of CNNs that operate in the spatial frequency domain as opposed to the conventional CNNs that operate with image pixels. For clarity, we refer to the former as *Spatial Frequency Convolutional Neural Networks (SF-CNN)*. SF-CNNs are formed by substituting the initial layers of standard CNN models with the spatial frequency (SF) layer that employs a spatial frequency extraction procedure. We will first describe the mechanism of the SF layer, then present the architecture of the SF-CNN models.

3.1. Spatial frequency layer

Here, we introduce the spatial frequency (SF) layer [15, 55], which employs a spatial frequency extraction procedure similar to the JPEG standard [51]. The SF layer transforms an $H \times W \times 3$ color image into an $H/8 \times W/8 \times 192$ output where the input image is split into 8×8 pixel blocks and each color channel of each pixel block is separately filtered by the Discrete Cosine Transform (DCT). DCT extracts the spatial frequencies along both horizontal and vertical directions. With the 8×8 pixel block represented by the matrix \mathbf{B} , DCT obtains an 8×8 frequency matrix \mathbf{D} as follows.

$$\mathbf{D}_{u,v} = \sum_{x=0}^7 \sum_{y=0}^7 \mathbf{B}_{x,y} \mathbf{K}_{x,y}^{u,v} \quad (1)$$

$$\mathbf{K}_{x,y}^{u,v} = \frac{c_u c_v}{4} \cos \left[\frac{(2x+1)u\pi}{16} \right] \cos \left[\frac{(2y+1)v\pi}{16} \right] \quad (2)$$

where u and v denote the horizontal and vertical spatial frequencies, respectively, and c_u is the normalizing factor equaling to $\frac{1}{\sqrt{2}}$ if the index $u = 0$, otherwise, $c_u = 1$. Afterwards, the frequency matrix \mathbf{D} is flattened into a 64-element vector by a zigzag pattern scan from low frequency to high frequency, and the flattened vectors of the three color channels of the same pixel block are concatenated together. Thus, the image is transformed from $(H, W, 3)$ to $(H/8, W/8, 3 \times 64)$ where H and W are the image height and the width, respectively.

The SF layer can be considered a particular case of applying convolutional layers with fixed weights $\mathbf{K}_{x,y}^{u,v}$.

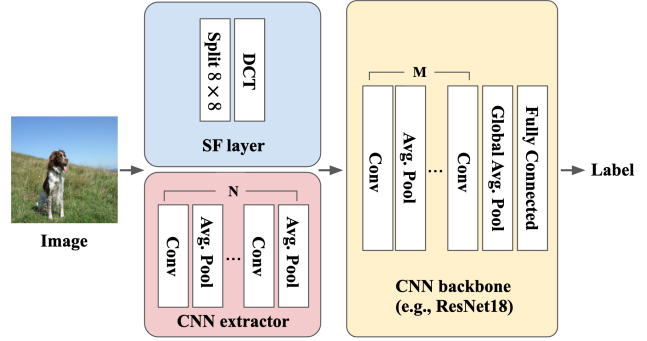


Figure 1: The comparison between SF-CNNs and standard CNNs. Standard CNNs utilize N trainable convolutional layers in the feature extractor and backbone classifier. SF-CNNs replace the feature extractor with the SF layer which conducts the block-wise DCT to extract the spatial frequencies as the initial image features but follows the same M -layer backbone architecture for classification.

Specifically, the above block-wise DCT process can be replicated by an 8×8 convolutional layer with stride 8 using Eq. (2) as the kernel weights. While the SF layer shares a similar function space as convolutional layers, our subsequent experiments demonstrate that SF-CNNs learn more robust parameters than standard CNNs because the SF layer can retain more low-frequency patterns (detailed in Sec. 5).

3.2. Spatial frequency CNN

To create the SF-CNNs, we modify widely-used CNN architectures by replacing the first few layers of each experimented model with the SF layer. In particular, by modifying *i) ResNet18*[16], *ii) EfficientNet*[45] and *iii) DenseNet*[19], we create SF-ResNet18, SF-DenseNet, and SF-EfficientNet, which are employed in the following adversarial robustness evaluations. In addition, SF-VGG11 is created from VGG11 [42] for a basic CNN model to be utilized in the transfer attack experiments. The modification guidelines are introduced as follows. We consider the SF layer to be a feature extractor with 192 different filters, corresponding to the different (block-wise) spatial frequencies of the three color spaces. Fig. 1 compares the SF-CNN with conventional CNN. Since most CNN model designs have monotonically increasing channel numbers for deeper layers [17], we replace the first few convolutional layers with less than 192 channels from the original CNN model with the SF layer. The subsequent layer would receive a 192 channel input instead of the original number. Due to space constraints, details of each experimented model architecture are provided in Appendix A.

4. Adversarial robustness of SF-CNN

In this section, we examine the performance and the robustness of SF-CNNs under both white-box and black-box attacks. While black-box attacks can be categorized into transfer attacks [7] or query-based attacks [48], the latter follows the PGD framework but estimates the gradient with zero-order queries. Thus, we focus on the transfer attack to evaluate different types of adversarial threats. We utilize *i) imagenette* [18] which selects 10 distinct and easily identifiable classes out of the total 1000 classes, as well as *ii) CIFAR10* [26] with 10 classes of tiny images and *iii) Flower102* [33] with 102 flower categories of large images to assert the generality of our observations. We split each dataset by 80%, 10%, and 10%, for training, validation, and testing, respectively.³ By default, we perform 100-step PGD attacks for thorough evaluations of model robustness in terms of accuracy. All model parameters are initialized with the Glorot initialization [12] and trained by the Adam optimizer with the default hyperparameter settings [25]. The training and evaluation procedures are implemented on an HP DL580 Gen 9 server with four 3.0 GHz Intel CPUs, 1TB RAM, and 8 Titan RTX 3080ti GPUs.

4.1. Robustness against white-box attacks

To analyze the robustness of SF-CNNs, we follow the standard adversarial robustness evaluation protocol to utilize PGD attacks [56], which generates the adversarial examples in an iterative gradient optimization process, in both pixel domain and frequency domain.

4.1.1 Perturbation in the pixel domain

In the following, we first follow a conventional attack schemes [14] to perturb the original images on its pixel values. Given the target classifier model C , the norm-bounded attack aims to find an adversarial example x^* for a given test image x such that,

$$C(x^*) \neq C(x), \text{ s.t. } x^* \in [0, 1]^N \cap \|x^* - x\|_\infty \leq \epsilon, \quad (3)$$

where $[0, 1]^N$ indicates that each of the N pixels is in the legitimate range of values. Note that $\|x^* - x\|_\infty \leq \epsilon$ restricts the modification to the test image to be human-imperceptible. We denote the union of the two limits as the adversarial limit $\Omega_\epsilon \equiv [0, 1]^N \cap \|x^* - x\|_\infty \leq \epsilon$. With full knowledge of the model weights, the PGD attack generates adversarial examples with the following iterative scheme:

$$x_{t+1}^* = \Pi_{\Omega_\epsilon}(x_t^* + \eta \text{sign}(\nabla \mathcal{L}(C, x_t^*, y))), \quad (4)$$

where t is the count of iteration with x_0^* being the original test image, Π_{Ω_ϵ} is the projection operation that projects

³To ensure integral division, the image datasets are reshaped to multiples of 8, where the ImageNet, CIFAR10, and Flower102 images are resized to (256×256) , (96×96) and (320×320) , respectively.

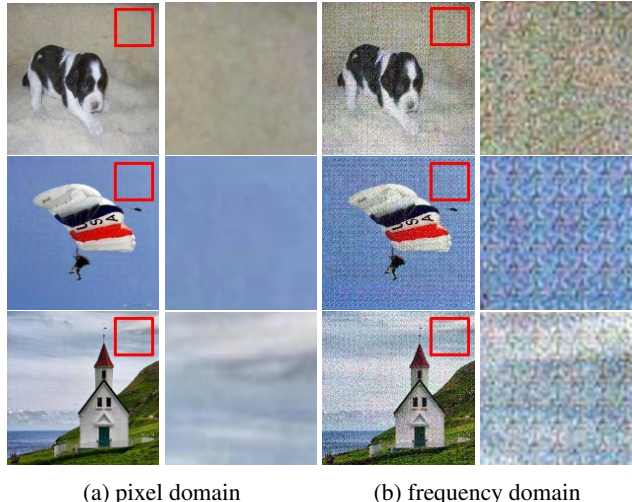


Figure 2: Examples of adversarial attacks in the pixel or the frequency domain with ϵ and ϵ_f set to 0.01. Perturbation on the frequency domain leaves a more visible adversarial noise with a periodic pattern.

the adversarial example back to the adversarial limit, η is the step size, $\nabla \mathcal{L}$ is the gradient of the relevant attack loss function, and y is the correct classification $C(x_0^*) = y$.

Following [50], we set $\epsilon = 0.003$ and $\epsilon = 0.01$ with $\eta = 0.001$ and 0.003 , respectively. Table 1 shows that all SF-CNN models trained in all datasets are more robust than their CNN counterparts. In particular, SF-DenseNet trained in the CIFAR10 dataset presents a drastic 38.8% increase in accuracy under $\epsilon = 0.003$ attack without utilizing any adversarial defense methods. The result supports the idea of improving the adversarial robustness of CNNs by mimicking the HVS to utilize spatial frequency channels. Moreover, since the SF-CNN models significantly reduce the parameter size by removing several layers from the CNN model (Fig. 1) but maintains similar test accuracy, we conclude that spatial frequency features provide sufficient semantic information for the model to learn.

4.1.2 Perturbation in the frequency domain

Next, we probe the SF-CNNs by perturbing the spatial frequencies f , *i.e.*, the output of the SF layer, directly, as:

$$C(x^*) \neq C(x), \text{ s.t. } x^* \in [0, 1]^N \cap \|f^* - f\|_\infty \leq \epsilon_f, \quad (5)$$

where f^* denotes the block-wise spatial frequencies of x^* . Similar to attacking in the pixel domain, we limit the perturbation by an ϵ_f , and utilize the PGD attack to generate adversarial examples.

As shown in Table 2, we report that although SF-CNNs perform better than CNNs in several combinations, attacking in the frequency domain are successful in most cases

model	ImageNette			CIFAR10			Flower102		
	Acc.	$\epsilon = 0.003$	$\epsilon = 0.01$	Acc.	$\epsilon = 0.003$	$\epsilon = 0.01$	Acc.	$\epsilon = 0.003$	$\epsilon = 0.01$
SF-VGG11	78.8%	63.6%	33.8%	78.6%	62.2%	42.0%	70.1%	54.7%	24.5%
VGG11	78.6%	60.2%	21.0%	79.0%	61.4%	27.8%	70.9%	0.0%	0.0%
SF-ResNet18	80.8%	67.2%	31.4%	78.0%	62.7%	26.4%	75.1%	61.7%	29.7%
ResNet18	80.2%	57.6%	14.4%	78.0%	60.8%	24.1%	74.0%	58.9%	16.4%
SF-EfficientNet	74.0%	58.2%	21.6%	77.0%	52.9%	8.6%	80.1%	55.2%	10.0%
EfficientNet	74.0%	45.4%	2.8%	79.8%	26.8%	0.2%	81.2%	43.8%	3.4%
SF-DenseNet	78.2%	61.2%	28.2%	77.1%	58.4%	18.5%	73.0%	60.8%	32.6%
DenseNet	78.2%	60.2%	25.6%	79.2%	19.6%	0.8%	71.4%	53.9%	14.8%

Table 1: Model performances under PGD attack in the pixel domain. ‘‘Acc.’’ denotes the test accuracy on clean images.

model \ ϵ_f	ImageNette		CIFAR10		Flower102	
	0.003	0.01	0.003	0.01	0.003	0.01
SF-VGG11	1.0%	0.0%	11.5%	0.0%	6.5%	3.4%
VGG11	0.0%	0.0%	0.0%	0.0%	0.0%	0.0%
SF-ResNet18	5.6%	0.0%	17.5%	0.1%	21.5%	0.0%
ResNet18	0.0%	0.0%	0.0%	0.0%	0.0%	0.0%
SF-EfficientNet	8.8%	0.2%	1.5%	0.0%	29.2%	0.1%
EfficientNet	0.0%	0.0%	0.0%	0.0%	0.1%	0.0%
SF-DenseNet	5.4%	0.2%	0.0%	0.0%	49.5%	5.6%
DenseNet	0.6%	0.0%	0.0%	0.0%	0.0%	0.0%

Table 2: Model performances under PGD attack in the frequency domain with $\epsilon_f = 0.003$ or 0.01 .

where the accuracy of SF-CNNs and CNNs are both reduced to 0%. Particularly, the accuracy of CNNs are overall lower than 0.6% while the accuracy of SF-CNNs are less than 49.5% with $\epsilon_f = 0.003$ and less than 8.8% with $\epsilon_f = 0.01$. However, we report that the ϵ_f -bound corresponds to pixel differences that greatly exceed a corresponding ϵ -bound. For instance, perturbing within $\epsilon_f = 0.003$ of the frequency range results in a maximum of 0.122 change in the pixel values. Fig. 2 also shows that such attacks leave distinct patterns that are visually observable in the adversarial examples.

By inspecting the frequency value distribution, we also find that attacking in the frequency domain create a significant shift in the spatial frequency value distribution, such that adversarial examples can be easily detected with a 100% detection rate. In particular, while the distribution of frequency components forms a peak at the zero value, adversarial examples created by the PGD attack in the frequency domain shows two peaks corresponding to the ϵ_f limit. Details of a basic detection method based on distribution of frequency values are reported in Appendix B.1.

model	Acc.	$\epsilon = 0.1$	$\epsilon = 0.2$	$\epsilon = 0.3$
SF-VGG11	78.8%	73.8%	57.8%	44.2%
VGG11	78.6%	0.0%	0.0%	0.0%
SF-ResNet18	80.8%	72.2%	49.0%	31.2%
ResNet18	80.2%	52.2%	26.6%	16.0%
SF-EfficientNet	74.2%	65.8%	42.2%	19.4%
EfficientNet	74.0%	63.6%	39.0%	16.8%
SF-DenseNet	78.2%	72.8%	60.2%	40.8%
DenseNet	78.2%	60.8%	24.8%	11.8%

Table 3: Model performances under transfer attack from VGG11. SF-CNNs are much more robust than CNNs.

model	Acc.	$\epsilon = 0.1$	$\epsilon = 0.2$	$\epsilon = 0.3$
SF-VGG11	80.2%	0.0%	0.0%	0.0%
VGG11	78.6%	61%	25.8%	17%
SF-ResNet18	80.8%	73.8%	58.8%	38.2%
ResNet18	80.2%	69.2%	37%	14.6%
SF-EfficientNet	74.2%	64.6%	61.4%	56.2%
EfficientNet	74.0%	72.8%	59%	41.2%
SF-DenseNet	78.2%	72.0%	66.0%	58.4%
DenseNet	78.2%	68.6%	35.6%	17.4%

Table 4: Model performances under transfer attack from SF-VGG11. Remarkably, SF-CNNs are more robust.

4.2. Robustness against transfer attack

Transferability of adversarial examples among CNN models is a well-known issue [14], leading to the possibility of *transfer attacks* [7]. In the following, we compare the robustness of SF-CNN and CNN models to adversarial examples generated by a VGG11 model or a SF-VGG11 model using transfer attacks. In particular, the compared models including VGG11 and SF-VGG11 are all trained in the imagenette dataset, and the adversarial examples are created with PGD attacks.

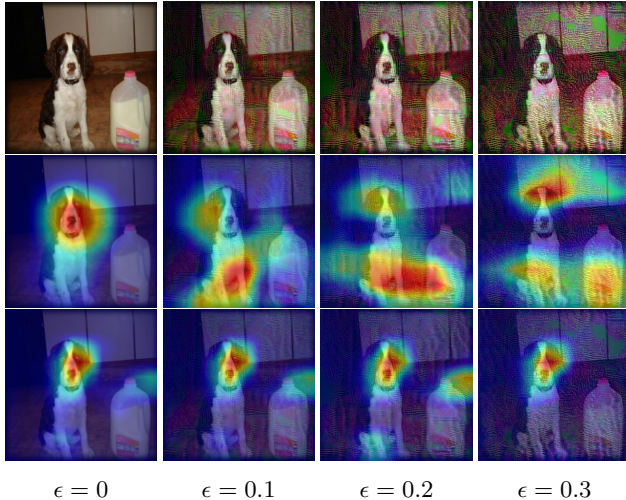


Figure 3: Grad-Cam visualizations of transfer attacks from VGG11. Top, middle, and bottom rows present the images, Grad-Cam visualization of ResNet18, and that of SF-ResNet18, respectively.

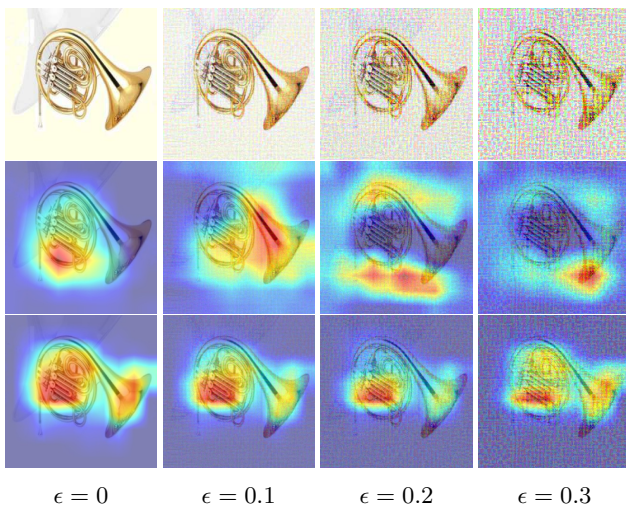


Figure 4: Grad-Cam visualizations of transfer attacks from SF-VGG11. Top, middle, and bottom rows present the images, Grad-Cam visualization of ResNet18, and that of SF-ResNet18, respectively.

4.2.1 Transfer attacks from VGG11

As shown in Table 3, the model accuracy under transfer attacks from VGG11 is significantly *higher* for all SF-CNN models compared to their CNN model counterparts. In particular, VGG11 models have 0% accuracy since the adversarial examples are generated from the same models. However, transferring the same adversarial examples to SF-VGG11 remarkably find 73.8%, 57.8% and 44.2% under $\epsilon = 0.1, 0.2$ and 0.3 , respectively. SF-ResNet18,

SF-EfficientNet, and SF-DenseNet also on average enjoy 42.6%, 6.3%, and 56.9% better accuracy under transfer attack, compared to ResNet18, EfficientNet, and DenseNet, respectively. A potential explanation can be found by inspecting the difference between the frequency domain and the image pixel domain. In particular, the basis of the frequency domain and the original image pixel domain are nearly orthogonal since the basis of the frequency domain corresponds to cosine values of different frequencies spanning the 8 pixels in Eq. (2), whereas the basis of the pixel domain corresponds to each pixel. Note that we utilize ϵ values larger than the usual 0.03 [54] to thoroughly compare SF-CNNs' and CNNs' resistance towards transfer attacks.

By comparing Grad-CAM visualizations [39] of the model attention of SF-ResNet18 and that of ResNet18 on the adversarial examples, we find that SF-CNNs indeed learn a different set of features by operating in the spatial frequency domain. As shown in Fig. 3, initially, both SF-ResNet18 and ResNet18 focus on the same semantic regions to correctly classify the clean test image. As the adversarial perturbation increases along with the ϵ value, the adversarial pattern begins to divert ResNet18's attention towards other regions, such that it could not focus on the correct regions. However, despite the intense adversarial noises, SF-ResNet18's attention maintains roughly at the same place and could still correctly classify the adversarial example. Such a result indicates that adversarial patterns that can fool CNNs are mostly neglected by SF-CNNs, allowing SF-CNNs to be robust against transfer attacks.⁴

4.2.2 Transfer attacks from SF-VGG11

Table 4 presents the results of the transfer attacks from SF-VGG11. Remarkably, all SF-CNN models (except SF-VGG11 itself) perform better than their CNN counterparts. In other words, the SF-CNN models are manipulated by adversarial perturbations targeting SF-VGG11 *less* than CNN models. Indeed, Grad-CAM visualizations (Fig. 4) for transfer attacks from SF-VGG11 show similar trend as Fig. 3, where the attention of SF-ResNet18 is less affected by the adversarial patterns than ResNet18. Such a result suggests that SF-CNN models are overall more robust against transfer attacks than CNN models. In addition, the lack of transferability across SF-CNNs indicates that different features are learned by SF-CNN models using different architectures. As such, SF-CNNs present a unique advantage under the black-box setting: while an adversary may choose any CNN architecture as a surrogate model to generate a successful transfer attack, the same adversary is required to select the correct baseline architecture when facing an SF-CNN model.

⁴Grad-CAM visualizations of more models for both transfer attacks from VGG11 and SF-VGG11 are provided in Appendix B.3.

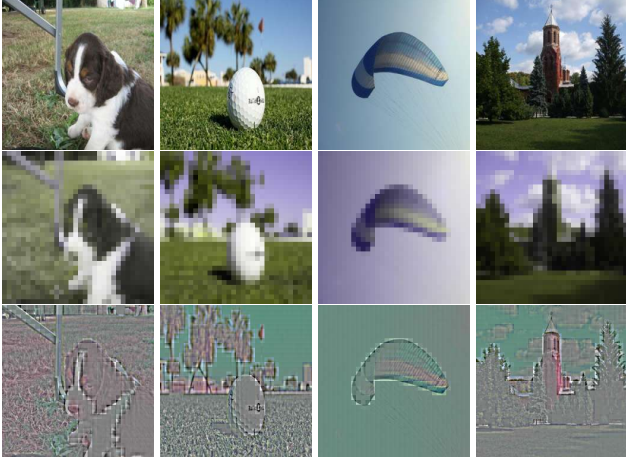


Figure 5: Examples of the original image (top), LFR (middle) and HFR (bottom). Despite using only the lowest frequency components, LFRs are visually more similar to the original images than HFRs.

model	ALL	HFR	LFR	ALL-ADV	HFR-ADV	LFR-ADV
SF	80.8%	25.8%	54.6%	47.2%	20.3%	39.9%
C_{88}	79.6%	42.9%	49%	5.8%	14.3%	45.2%

Table 5: Comparing SF-ResNet18 and C_{88} -ResNet18 model accuracy on high or low frequency reconstructions of clean or adversarial examples ($\epsilon = 0.01$) of imagenette.

5. Further analysis of SF Layer

In this section, we analyze the effect of the initial feature extraction layer by comparing the SF layer with an equivalently sized convolutional layer C_{88} . Concretely, C_{88} layer is an 8×8 stride 8 convolutional layer with 3 input and 192 output channels. For a fair comparison, we construct a C_{88} -ResNet18 with identical architecture as SF-ResNet18 except for the first feature extraction layer.

5.1. The impact of image frequency

We compare SF-ResNet18’s and C_{88} -ResNet18’s responses to the frequency-based reconstruction of clean and adversarial images [52]. As shown in Fig. 5, we separate the lowest frequency, *i.e.*, $D_{0,0}$ in Eq. (1), for each pixel patch and color of the original image (ALL) to reconstruct the low-frequency image (LFR), and all other frequencies for the high-frequency image (HFR). We repeat the same process on the adversarial examples (ALL-ADV) for the low- (LFR-ADV) and high-frequency reconstructions (HFR-ADV).

In Table 5, we find that C_{88} -ResNet18 shows higher accuracy on HFR, which indicates that the model relies more on the high-frequency information. In contrast, an SF-ResNet18 appears to utilize the lowest frequency component more, since the model has higher accuracy on

α	0	1/4	1/2	3/4	1
Acc.	79.6%	78.8%	78.2%	79.0%	80.8%
$\epsilon = 0.003$	47.2%	60.0%	62.4%	64.8%	67.2%
$\epsilon = 0.01$	5.8%	21.2%	24.0%	28.8%	31.2%

Table 6: Performances of the interpolation models with different α values.

β	0	1/64	1/16	1/4	1
Acc.	79.6%	79.4%	78.6%	78.6%	80.8%
$\epsilon = 0.003$	47.2%	65.8%	65.6%	66.0%	67.2%
$\epsilon = 0.01$	5.8%	26.4%	26.8%	30.8%	31.2%

Table 7: Performances of the substitution models with different β values.

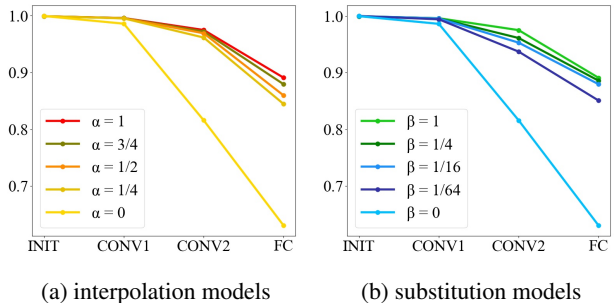


Figure 6: The average cosine similarity of each layer outputs between clean images and the corresponding adversarial examples. Higher cosine similarity indicates less effect from the adversarial perturbation on the layer activation, corresponding to better adversarial robustness.

LFR. Comparing HFR-ADV and LFR-ADV, both models obtain weaker performance with HFR-ADV than LFR-ADV, indicating that the harm of adversarial examples comes more from their high-frequency components than the low-frequency components. Since SF-ResNet18 utilizes more low-frequency patterns, it remains more robust than C_{88} -ResNet18 against adversarial attacks. Note that SF-ResNet18 shows better accuracy over C_{88} -ResNet18 in ALL-ADV by utilizing the information in LFR-ADV. In Fig. 5, LFR is visually more similar to the original image than HFR for a human observer.

5.2. Mixture models of SF and C_{88} layers

To validate the robustness of different feature extractors, we conduct additional experiments with two types of mixture models between SF-ResNet18 and C_{88} -ResNet18.

5.2.1 Interpolation model

First, we introduce an *interpolation model* between SF-ResNet18 and C_{88} -ResNet18 by interpolating the first layer between the SF layer and the C_{88} layer as follows:

$$\mathbf{K}_{inter} = \alpha \mathbf{K}_{SF} + (1 - \alpha) \mathbf{K}_{88}, \alpha \in [0, 1], \quad (6)$$

where \mathbf{K}_{88} and \mathbf{K}_{SF} denote the kernel weights of C_{88} layer and SF layer, respectively. As such, the interpolation model begins as C_{88} model and gradually becomes an SF-model as the portion α increases.

Table 6 shows that the interpolation models are most robust when $\alpha = 1$ (corresponding to SF-ResNet18), and least robust when $\alpha = 0$ (corresponding to C_{88} -ResNet18). The accuracy of the interpolation model consistently improves as α increases from 0 to 1. It manifests that the SF layer could extract more robust features than the C_{88} layer. To further understand the effect of feature extraction, we measure the average cosine similarity between the layer outputs of clean and adversarial images at 1) the first layer INIT (*i.e.*, Eq. (6)), 2) the first residual block CONV1, 3) the second residual block CONV2, and 4) the final fully connected layer FC (see Appendix A for detail).

The result in Fig. 6a suggests that the adversarial attack process locates an adversarial pattern that is amplified along each consecutive layer. Since the adversarial pattern is bounded by an ϵ limit, the cosine similarity between the adversarial image and the clean image is approximately 1. Then, after being processed by the initial feature extraction layer (INIT) and the first convolutional block (CONV1), the layer output for the clean and adversarial examples begin to differ, leading to a decrease in their cosine similarity. Subsequent layer processes (CONV2 and FC) show even larger deviations. Note that while the cosine similarity at the last layer maintains at 0.89 for SF-ResNet18 ($\alpha = 1$), the corresponding value dropped to 0.63 for C_{88} -ResNet18 ($\alpha = 0$). In particular, the cosine similarity in the last layer FC of the $\alpha = 0$ model is significantly lower than other interpolation models, while $\alpha = 0$ also corresponds to the interpolation model with no contributions from the SF layer. Thus, we conclude that training on a *good* initial feature extraction layer, *i.e.*, the SF layer leads to a more robust model weight in the subsequent layers, such that the layer output differences caused by the adversarial perturbations are less severe.

5.2.2 Substitution model

To further evaluate the effect of each channel in SF layer, we propose the *substitution model* which is constructed by replacing the kernels of the C_{88} layer with that of the SF layer by the portion β , which can be defined as follows:

$$\mathbf{K}_{sub} = \text{concat}(\mathbf{K}_{SF}[\beta \cdot 192:], \mathbf{K}_{88}[\beta \cdot 192:]), \beta \in [0, 1], \quad (7)$$

where $\text{concat}(\cdot)$ denotes the concatenation operation of two matrices. Thus, our \mathbf{K}_{sub} has 192 channels, which is identical to both the SF layer and the C_{88} layer. Note that we sort the SF layer kernels from the low frequency to the high frequency, *i.e.*, $\mathbf{K}_{SF}[0]$ is the lowest frequency channel, and $\mathbf{K}_{SF}[191]$ represents the highest frequency. As β increases, we gradually replace the kernels in C_{88} with the low-frequency kernels from the SF layer.

Table 7 shows a similar trend as the interpolation models in Table 6, where the substitution model is most robust when $\beta = 1$ (corresponding to SF-ResNet18), and least robust when $\beta = 0$ (corresponding to C_{88} -ResNet18). After adding the lowest frequency channel, *i.e.*, with $\beta = 1/64$, the model performance significantly improves by 39.4% and 355.6% in terms of test accuracy for $\epsilon = 0.003$ and $\epsilon = 0.001$, respectively. Afterward, the model continues to improve as β increases. As an additional experiment, adding the 1/4 highest frequency channels of SF layer shows less promising results of 54.4% with $\epsilon = 0.003$ and 10.1% with $\epsilon = 0.01$. In contrast, adding 1/4 lowest frequency channels of SF layer finds 66.0% ($\epsilon = 0.003$) and 30.8% ($\epsilon = 0.01$). Such comparison manifests that low-frequency components of the SF layer significantly contribute to the adversarial robustness of SF-CNN models. Moreover, we also measure the cosine similarities between model responses of clean and perturbed images for the substitution models in Fig. 6b, and observe the same cosine similarity drop along the layers. Moreover, the cosine similarity of the last layer FC of $\beta = 0$ is significantly lower than other β values. By comparing $\beta = 0$ with $\beta = 1/64$ in both Fig. 6b and Table 7, we observe that substituting the *lowest frequencies* alone causes the most significant improvements in terms of adversarial robustness. Substituting higher frequency kernels in addition only amounts to slight improvements. Such an observation supports the hypothesis that SF-CNNs gain robustness by utilizing the lower frequency components, as suggested in Table 5.

6. Conclusions

This work presents an empirical study exploring the adversarial robustness of CNNs operating in the spatial frequency domain. We propose the SF layer, which extracts spatial frequency components, and replace the first few layers of popular CNN models with the SF layer to obtain the SF-CNNs. SF-CNNs are significantly more robust than their CNN counterparts under white-box and black-box attacks. Further comparisons between the SF layer and a trainable CNN layer manifest the importance of the initial feature extraction layer, where the low-frequency filters play a crucial role in the adversarial robustness. We believe our discoveries provide insights into the nature of adversarial examples and may be utilized in future work to develop defensive methods against adversarial attacks.

References

- [1] Nasir Ahmed, T. Natarajan, and Kamisetty R Rao. Discrete cosine transform. *IEEE transactions on Computers*, 100(1):90–93, 1974.
- [2] Anish Athalye, Nicholas Carlini, and David Wagner. Obfuscated gradients give a false sense of security: Circumventing defenses to adversarial examples. In *International conference on machine learning*, pages 274–283. PMLR, 2018.
- [3] Nicholas Carlini and David Wagner. Towards evaluating the robustness of neural networks. In *2017 IEEE Symposium on Security and Privacy (SP)*, pages 39–57. IEEE, 2017.
- [4] Wenlin Chen, James Wilson, Stephen Tyree, Kilian Q Weinberger, and Yixin Chen. Compressing convolutional neural networks in the frequency domain. In *Proceedings of the 22nd ACM SIGKDD international conference on knowledge discovery and data mining*, pages 1475–1484, 2016.
- [5] Francesco Croce, Maksym Andriushchenko, Vikash Sehrawag, Edoardo Debenedetti, Nicolas Flammarion, Mung Chiang, Prateek Mittal, and Matthias Hein. Robustbench: a standardized adversarial robustness benchmark. *arXiv preprint arXiv:2010.09670*, 2020.
- [6] Joel Dapello, Tiago Marques, Martin Schrimpf, Franziska Geiger, David Cox, and James J DiCarlo. Simulating a primary visual cortex at the front of cnns improves robustness to image perturbations. *Advances in Neural Information Processing Systems*, 33:13073–13087, 2020.
- [7] Ambra Demontis, Marco Melis, Maura Pintor, Matthew Jagielski, Battista Biggio, Alina Oprea, Cristina Nita-Rotaru, and Fabio Roli. Why do adversarial attacks transfer? explaining transferability of evasion and poisoning attacks. In *28th USENIX security symposium (USENIX security 19)*, pages 321–338, 2019.
- [8] Russell L DeValois, Karen K De Valois, and Karen K DeValois. *Spatial vision*. Number 14. Oxford University Press on Demand, 1990.
- [9] Minjing Dong, Yunhe Wang, Xinghao Chen, and Chang Xu. Towards stable and robust addernets. *Advances in Neural Information Processing Systems*, 34:13255–13265, 2021.
- [10] Max Ehrlich and Larry S Davis. Deep residual learning in the jpeg transform domain. In *Proceedings of the IEEE International Conference on Computer Vision*, pages 3484–3493, 2019.
- [11] Robert Geirhos, Patricia Rubisch, Claudio Michaelis, Matthias Bethge, Felix A. Wichmann, and Wieland Brendel. Imagenet-trained CNNs are biased towards texture; increasing shape bias improves accuracy and robustness. In *International Conference on Learning Representations*, 2019.
- [12] Xavier Glorot and Yoshua Bengio. Understanding the difficulty of training deep feedforward neural networks. In *Proceedings of the thirteenth international conference on artificial intelligence and statistics*, pages 249–256. JMLR Workshop and Conference Proceedings, 2010.
- [13] Ian Goodfellow. Defense against the dark arts: An overview of adversarial example security research and future research directions. *arXiv preprint arXiv:1806.04169*, 2018.
- [14] Ian J Goodfellow, Jonathon Shlens, and Christian Szegedy. Explaining and harnessing adversarial examples. In *International Conference on Learning Representations*, 2015.
- [15] Lionel Gueguen, Alex Sergeev, Ben Kadlec, Rosanne Liu, and Jason Yosinski. Faster neural networks straight from jpeg. *Advances in Neural Information Processing Systems*, 31, 2018.
- [16] Kaiming He, Xiangyu Zhang, Shaoqing Ren, and Jian Sun. Deep residual learning for image recognition. In *Proceedings of the IEEE conference on computer vision and pattern recognition*, pages 770–778, 2016.
- [17] Byeongho Heo, Sangdoon Yun, Dongyoon Han, Sanghyuk Chun, Junsuk Choe, and Seong Joon Oh. Rethinking spatial dimensions of vision transformers. In *Proceedings of the IEEE/CVF International Conference on Computer Vision*, pages 11936–11945, 2021.
- [18] Jeremy Howard. Imagenette.
- [19] Gao Huang, Zhuang Liu, Laurens Van Der Maaten, and Kilian Q Weinberger. Densely connected convolutional networks. In *Proceedings of the IEEE conference on computer vision and pattern recognition*, pages 4700–4708, 2017.
- [20] Jiaying Huang, Dayan Guan, Aoran Xiao, and Shijian Lu. Fsd: Frequency space domain randomization for domain generalization. In *Proceedings of the IEEE/CVF Conference on Computer Vision and Pattern Recognition*, pages 6891–6902, 2021.
- [21] Jiaying Huang, Dayan Guan, Aoran Xiao, and Shijian Lu. Rda: Robust domain adaptation via fourier adversarial attacking. In *Proceedings of the IEEE/CVF International Conference on Computer Vision*, pages 8988–8999, 2021.
- [22] Andrew Ilyas, Shibani Santurkar, Dimitris Tsipras, Logan Engstrom, Brandon Tran, and Aleksander Madry. Adversarial examples are not bugs, they are features. *Advances in neural information processing systems*, 32, 2019.
- [23] Nathan Inkawhich, Wei Wen, Hai Helen Li, and Yiran Chen. Feature space perturbations yield more transferable adversarial examples. In *Proceedings of the IEEE/CVF Conference on Computer Vision and Pattern Recognition*, pages 7066–7074, 2019.
- [24] Qiyu Kang, Yang Song, Qinxu Ding, and Wee Peng Tay. Stable neural ode with lyapunov-stable equilibrium points for defending against adversarial attacks. *Advances in Neural Information Processing Systems*, 34:14925–14937, 2021.
- [25] Diederik P Kingma and Jimmy Ba. Adam: A method for stochastic optimization. *arXiv preprint arXiv:1412.6980*, 2014.
- [26] Alex Krizhevsky, Geoffrey Hinton, et al. Learning multiple layers of features from tiny images. 2009.
- [27] Andrew Lavin and Scott Gray. Fast algorithms for convolutional neural networks. In *Proceedings of the IEEE conference on computer vision and pattern recognition*, pages 4013–4021, 2016.
- [28] Yanpei Liu, Xinyun Chen, Chang Liu, and Dawn Song. Delving into transferable adversarial examples and black-box attacks. *arXiv preprint arXiv:1611.02770*, 2016.
- [29] Zhuang Liu, Hanzi Mao, Chao-Yuan Wu, Christoph Feichtenhofer, Trevor Darrell, and Saining Xie. A convnet for the

- 2020s. In *Proceedings of the IEEE/CVF Conference on Computer Vision and Pattern Recognition*, pages 11976–11986, 2022.
- [30] Aleksander Madry, Aleksandar Makelov, Ludwig Schmidt, Dimitris Tsipras, and Adrian Vladu. Towards deep learning models resistant to adversarial attacks. In *International Conference on Learning Representations*, 2018.
- [31] Najib J Majaj, Denis G Pelli, Peri Kurshan, and Melanie Palomares. The role of spatial frequency channels in letter identification. *Vision research*, 42(9):1165–1184, 2002.
- [32] Luis M Martinez and Jose-Manuel Alonso. Complex receptive fields in primary visual cortex. *The neuroscientist*, 9(5):317–331, 2003.
- [33] Maria-Elena Nilsback and Andrew Zisserman. Automated flower classification over a large number of classes. In *2008 Sixth Indian Conference on Computer Vision, Graphics & Image Processing*, pages 722–729. IEEE, 2008.
- [34] Nicolas Papernot, Patrick McDaniel, and Ian Goodfellow. Transferability in machine learning: from phenomena to black-box attacks using adversarial samples. *arXiv preprint arXiv:1605.07277*, 2016.
- [35] Zequn Qin, Pengyi Zhang, Fei Wu, and Xi Li. Fcanet: Frequency channel attention networks. In *Proceedings of the IEEE/CVF international conference on computer vision*, pages 783–792, 2021.
- [36] J. Ross Quinlan. Induction of decision trees. *Machine learning*, 1(1):81–106, 1986.
- [37] Joseph Redmon, Santosh Divvala, Ross Girshick, and Ali Farhadi. You only look once: Unified, real-time object detection. In *Proceedings of the IEEE conference on computer vision and pattern recognition*, pages 779–788, 2016.
- [38] Murray B Sachs, Jacob Nachmias, and John G Robson. Spatial-frequency channels in human vision. *JOSA*, 61(9):1176–1186, 1971.
- [39] Ramprasaath R Selvaraju, Michael Cogswell, Abhishek Das, Ramakrishna Vedantam, Devi Parikh, and Dhruv Batra. Grad-cam: Visual explanations from deep networks via gradient-based localization. In *Proceedings of the IEEE international conference on computer vision*, pages 618–626, 2017.
- [40] Ali Shafahi, Mahyar Najibi, Mohammad Amin Ghiasi, Zheng Xu, John Dickerson, Christoph Studer, Larry S Davis, Gavin Taylor, and Tom Goldstein. Adversarial training for free! *Advances in Neural Information Processing Systems*, 32, 2019.
- [41] Xing Shen, Jirui Yang, Chunbo Wei, Bing Deng, Jianqiang Huang, Xian-Sheng Hua, Xiaoliang Cheng, and Kewei Liang. Dct-mask: Discrete cosine transform mask representation for instance segmentation. In *Proceedings of the IEEE/CVF Conference on Computer Vision and Pattern Recognition*, pages 8720–8729, 2021.
- [42] Karen Simonyan and Andrew Zisserman. Very deep convolutional networks for large-scale image recognition. *arXiv preprint arXiv:1409.1556*, 2014.
- [43] David Stutz, Matthias Hein, and Bernt Schiele. Disentangling adversarial robustness and generalization. In *Proceedings of the IEEE/CVF Conference on Computer Vision and Pattern Recognition*, pages 6976–6987, 2019.
- [44] Christian Szegedy, Wojciech Zaremba, Ilya Sutskever, Joan Bruna, Dumitru Erhan, Ian Goodfellow, and Rob Fergus. Intriguing properties of neural networks. In *International Conference on Learning Representations*, 2014.
- [45] Mingxing Tan and Quoc Le. Efficientnetv2: Smaller models and faster training. In *International Conference on Machine Learning*, pages 10096–10106. PMLR, 2021.
- [46] Florian Tramer, Nicholas Carlini, Wieland Brendel, and Aleksander Madry. On adaptive attacks to adversarial example defenses. *Advances in Neural Information Processing Systems*, 33:1633–1645, 2020.
- [47] Dimitris Tsipras, Shibani Santurkar, Logan Engstrom, Alexander Turner, and Aleksander Madry. Robustness may be at odds with accuracy. In *International Conference on Learning Representations*, 2019.
- [48] Chun-Chen Tu, Paishun Ting, Pin-Yu Chen, Sijia Liu, Huan Zhang, Jinfeng Yi, Cho-Jui Hsieh, and Shin-Ming Cheng. Autozoom: Autoencoder-based zeroth order optimization method for attacking black-box neural networks. In *Proceedings of the AAAI Conference on Artificial Intelligence*, volume 33, pages 742–749, 2019.
- [49] Patrik Vuilleumier, Jorge L Armony, Jon Driver, and Raymond J Dolan. Distinct spatial frequency sensitivities for processing faces and emotional expressions. *Nature neuroscience*, 6(6):624–631, 2003.
- [50] Manish Reddy Vuyyuru, Andrzej Banburski, Nishka Pant, and Tomaso Poggio. Biologically inspired mechanisms for adversarial robustness. *Advances in Neural Information Processing Systems*, 33:2135–2146, 2020.
- [51] Gregory K Wallace. The jpeg still picture compression standard. *IEEE transactions on consumer electronics*, 38(1):xviii–xxxiv, 1992.
- [52] Haohan Wang, Xindi Wu, Zeyi Huang, and Eric P Xing. High-frequency component helps explain the generalization of convolutional neural networks. In *Proceedings of the IEEE/CVF Conference on Computer Vision and Pattern Recognition*, pages 8684–8694, 2020.
- [53] Eric Wong, Leslie Rice, and J Zico Kolter. Fast is better than free: Revisiting adversarial training. *arXiv preprint arXiv:2001.03994*, 2020.
- [54] Dongxian Wu, Shu-Tao Xia, and Yisen Wang. Adversarial weight perturbation helps robust generalization. *Advances in Neural Information Processing Systems*, 33:2958–2969, 2020.
- [55] Kai Xu, Minghai Qin, Fei Sun, Yuhao Wang, Yen-Kuang Chen, and Fengbo Ren. Learning in the frequency domain. In *Proceedings of the IEEE/CVF Conference on Computer Vision and Pattern Recognition*, pages 1740–1749, 2020.
- [56] Hongyang Zhang, Yaodong Yu, Jiantao Jiao, Eric Xing, Laurent El Ghaoui, and Michael Jordan. Theoretically principled trade-off between robustness and accuracy. In *International conference on machine learning*, pages 7472–7482. PMLR, 2019.

A. SF-CNN model details

We present the detail layer-by-layer design of the experimented CNN and SF-CNN model architectures in Table 9. Besides, the way to formulate the SF layer as a C_{88} layer are described as follows. A C_{88} layer is a convolutional layer with 192 instances of $3 \times 8 \times 8$ kernel filters. Since each kernel filter “sees” all three input channels (color space) at once, to create a convolutional layer with the same function as Eq. (2), which only processes one color, we fill two 8×8 layers with 0 and one layer with the $\mathbf{K}^{u,v}$ matrix with a particular set of u and v value. Thus, 3 color selections and 64 possible u, v results in 192 kernel filters, matching the dimensions of the C_{88} layer. Three kernels representing the same spatial frequency are grouped together and each frequency group is ordered by the zigzag scanning pattern shown in Fig. 7.

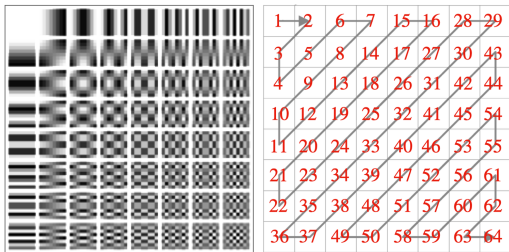


Figure 7: The DCT basis and the zigzag pattern

B. Additional Experiments

B.1. Detection of adversarial example

While the adversarial example can cause CNNs to misclassify and raise several concerns about models applicability, it is of paramount importance to develop detection methods for adversarial examples, thus allowing them to reject them. Fig. 8 compares the distribution of frequency component values and that of the pixel values.⁵ We observe that frequency value distribution for natural images forms a peak centered at 0. Noticeably, adversarial attacks in the pixel domain flatten the peak, whereas attacks in the frequency domain split into two peaks. In contrast, the same adversarial perturbations do not show simple patterns of change in the pixel values. Based on such observation, we preprocess the DCT coefficient of each image by dividing the range $[-3, 3]$ into 5 intervals and count the frequency components with values in each interval as the input feature. Then, we train a Decision Tree classifier [36] for detection, which is able to achieve 100% detection accuracy across all models (including standard CNNs and SF-CNNs) and datasets

⁵The distribution is plotted for an arbitrary image since all images show the same pattern between clean and adversarial examples.

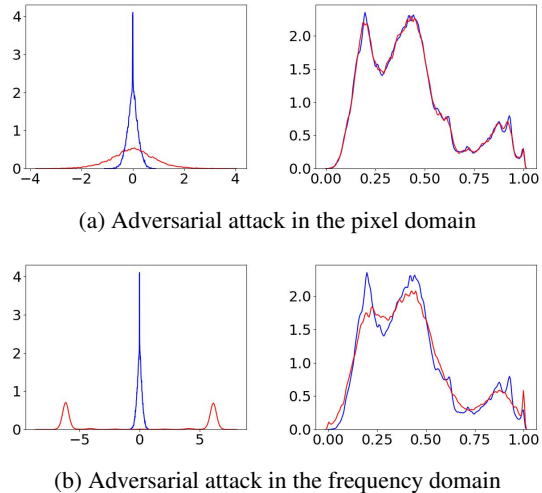


Figure 8: The distributions of frequency component values (left) and pixel values (right) of an adversarial example (red) and the original test image (blue). For adversarial attack in both the pixel domain and the frequency domain, the frequency value distributions show clear differences while the pixel values are ambiguous.

since the frequency distribution shifts shown in Fig. 8 are significant and universal.

B.2. Evaluation with adversarial training

We follow [40] to perform adversarial training with $\epsilon = 0.03$ adversarial examples. The same adversarial training procedure is applied to both SF-ResNet18 and ResNet18. As shown in Table 8, we observe that SF-CNNs are better or equal to CNNs under adversarial training while maintaining the same test accuracy. The result validates the efficacy of utilizing the frequency domain with adversarial training methods.

model	Acc.	$\epsilon = 0.003$	$\epsilon = 0.01$	$\epsilon = 0.03$
SF-ResNet18	76.2%	72.2%	65.4%	38.0%
ResNet18	76.2%	72.2%	63.4%	32.0%

Table 8: Attacked accuracy of adversarially trained SF-ResNet18 and ResNet18 on the imagenette dataset. “Acc.” denotes clean test accuracy.

B.3. More Grad-cam visualization results

Here, we provide the grad-cam visualizations of model attention for different CNN and SF-CNN models under transfer attacks from VGG11 in Fig. 9 and SF-VGG11 in Fig. 10. In both cases, SF-CNN models are consistently *more focused*, i.e., the greater attention weight on the ob-

ResNet18	SF-ResNet18	EfficientNet	SF-EfficientNet
$7 \times 7, 64, \text{stride}2$	} replaced with the SF layer	$3 \times 3, 24, \text{stride}2$	} replaced with the SF layer
$3 \times 3 \text{ max pool, stride } 2$		Fused-MBConv $3 \times 3, 24 \times 3$	
$\begin{bmatrix} 3 \times 3, 64 \\ 3 \times 3, 64 \end{bmatrix} \times 2$		Fused-MBConv $3 \times 3, 48 \times 5$	
$\begin{bmatrix} 3 \times 3, 128 \\ 3 \times 3, 128 \end{bmatrix} \times 2$		Fused-MBConv $3 \times 3, 80 \times 5$	
$\begin{bmatrix} 3 \times 3, 256 \\ 3 \times 3, 256 \end{bmatrix} \times 2$		MBConv $3 \times 3, 160 \times 7$	
$\begin{bmatrix} 3 \times 3, 512 \\ 3 \times 3, 512 \end{bmatrix} \times 2$	$\begin{bmatrix} 3 \times 3, 256 \\ 3 \times 3, 256 \end{bmatrix} \times 2$	MBConv $3 \times 3, 176 \times 14$	
$\begin{bmatrix} 3 \times 3, 512 \\ 3 \times 3, 512 \end{bmatrix} \times 2$	$\begin{bmatrix} 3 \times 3, 512 \\ 3 \times 3, 512 \end{bmatrix} \times 2$	MBConv $3 \times 3, 304 \times 18$	MBConv $3 \times 3, 304 \times 18$
$7 \times 7 \text{ average pool}$	$7 \times 7 \text{ average pool}$	MBConv $3 \times 3, 512 \times 5$	MBConv $3 \times 3, 512 \times 5$
512×10	512×10	$1 \times 1, 1792, \text{stride } 1$	$1 \times 1, 1792, \text{stride } 1$
		$1 \times 1 \text{ average pool}$	$1 \times 1 \text{ average pool}$
		1792×10	1792×10
DenseNet	SF-DenseNet	VGG11	SF-VGG11
$7 \times 7, 64, \text{stride}2$	SF layer	$3 \times 3, 64, \text{stride}2$	} replaced with the SF layer
$3 \times 3 \text{ max pool, stride } 2$	$7 \times 7, 192, \text{stride}2$	$2 \times 2 \text{ max pool, stride } 2$	
$\begin{bmatrix} 1 \times 1, 128 \\ 3 \times 3, 32 \end{bmatrix} \times 6$	$3 \times 3 \text{ max pool, stride } 2$	$3 \times 3, 128, \text{stride} = 1$	
$1 \times 1, 128$	$\begin{bmatrix} 1 \times 1, 128 \\ 3 \times 3, 32 \end{bmatrix} \times 6$	$2 \times 2 \text{ max pool, stride } 2$	
$2 \times 2 \text{ average pool, stride } 2$	$1 \times 1, 192$	$\begin{bmatrix} 3 \times 3, 256 \\ 3 \times 3, 256 \end{bmatrix} \times 2$	
$\begin{bmatrix} 1 \times 1, 128 \\ 3 \times 3, 32 \end{bmatrix} \times 12$	$2 \times 2 \text{ average pool, stride } 2$	$2 \times 2 \text{ max pool, stride } 2$	$\begin{bmatrix} 3 \times 3, 256 \\ 3 \times 3, 256 \end{bmatrix} \times 2$
$1 \times 1, 256$	$\begin{bmatrix} 1 \times 1, 128 \\ 3 \times 3, 32 \end{bmatrix} \times 12$	$2 \times 2 \text{ max pool, stride } 2$	$2 \times 2 \text{ max pool, stride } 2$
$2 \times 2 \text{ average pool, stride } 2$	$1 \times 1, 288$	$\begin{bmatrix} 3 \times 3, 512 \\ 3 \times 3, 512 \end{bmatrix} \times 2$	$\begin{bmatrix} 3 \times 3, 512 \\ 3 \times 3, 512 \end{bmatrix} \times 2$
$\begin{bmatrix} 1 \times 1, 128 \\ 3 \times 3, 32 \end{bmatrix} \times 24$	$2 \times 2 \text{ average pool, stride } 2$	$2 \times 2 \text{ max pool, stride } 2$	$2 \times 2 \text{ max pool, stride } 2$
$1 \times 1, 512$	$\begin{bmatrix} 1 \times 1, 128 \\ 3 \times 3, 32 \end{bmatrix} \times 24$	$\begin{bmatrix} 3 \times 3, 512 \\ 3 \times 3, 512 \end{bmatrix} \times 2$	$\begin{bmatrix} 3 \times 3, 512 \\ 3 \times 3, 512 \end{bmatrix} \times 2$
$2 \times 2 \text{ average pool, stride } 2$	$1 \times 1, 528$	$2 \times 2 \text{ max pool, stride } 2$	$2 \times 2 \text{ max pool, stride } 2$
$\begin{bmatrix} 1 \times 1, 128 \\ 3 \times 3, 32 \end{bmatrix} \times 16$	$2 \times 2 \text{ average pool, stride } 2$	$2 \times 2 \text{ max pool, stride } 2$	$2 \times 2 \text{ max pool, stride } 2$
$7 \times 7 \text{ global average pool}$	$\begin{bmatrix} 1 \times 1, 128 \\ 3 \times 3, 32 \end{bmatrix} \times 16$	4096×10	4096×10
1024×10	$7 \times 7 \text{ global average pool}$		
	1040×10		

Table 9: The CNN and SF-CNN model architectures. Here, $k \times k, h$ indicate convolution layer (if not specified as a pooling layer) with h output channels of $k \times k$ kernels with stride 1 (if stride not specified). Brackets denote residual blocks. The last layers are fully connected layers.

jects than their CNN counterparts. The visualizations support the claim that SF-CNNs learn a more robust set of features by operating in the spatial frequency domain.

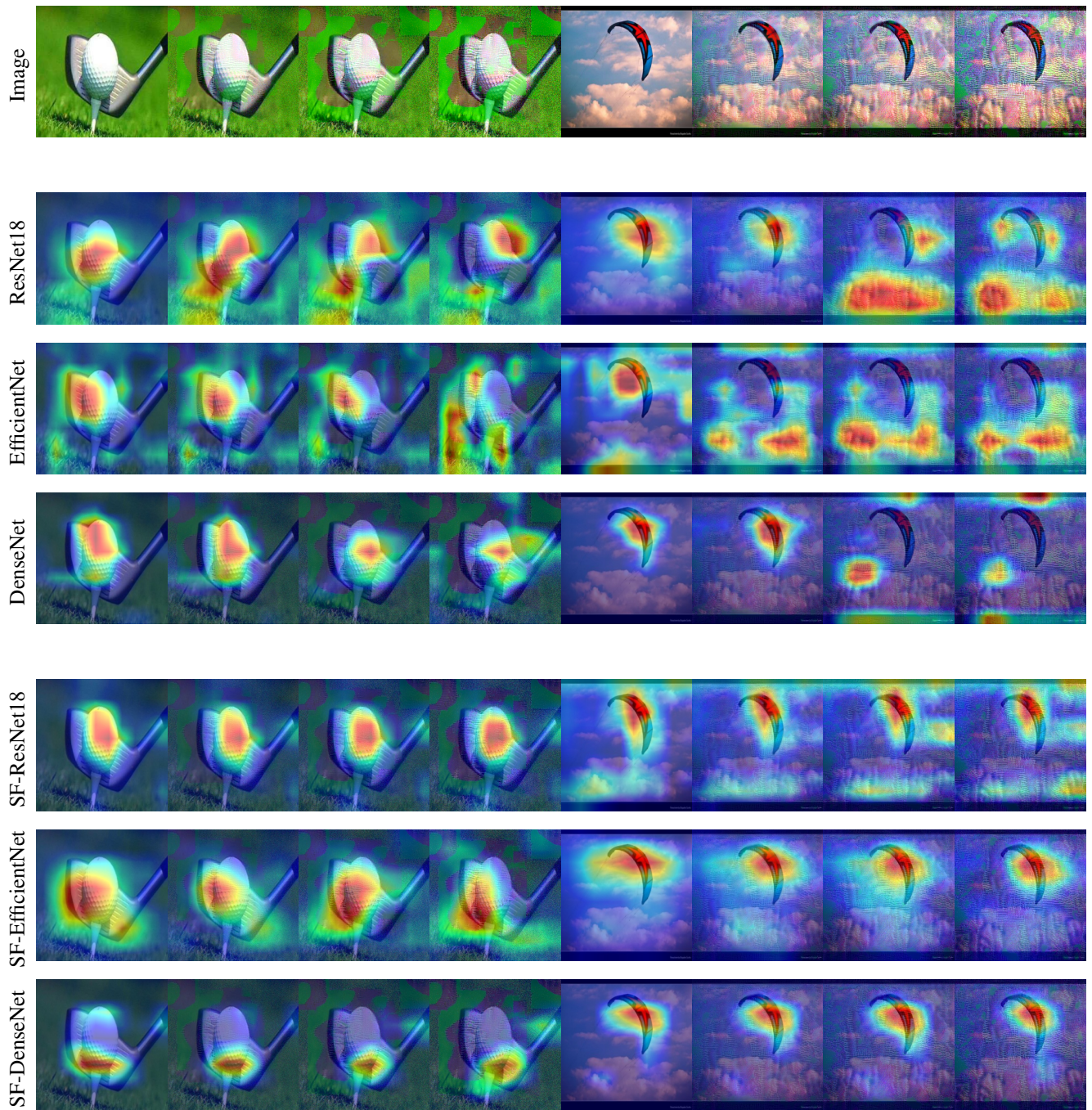


Figure 9: Grad-Cam visualizations of model attention on two adversarial examples generated from **VGG11**. Each row shows the progression from $\epsilon = 0$ (not attacked) to $\epsilon = 0.1, 0.2$ and 0.3 from left to right.

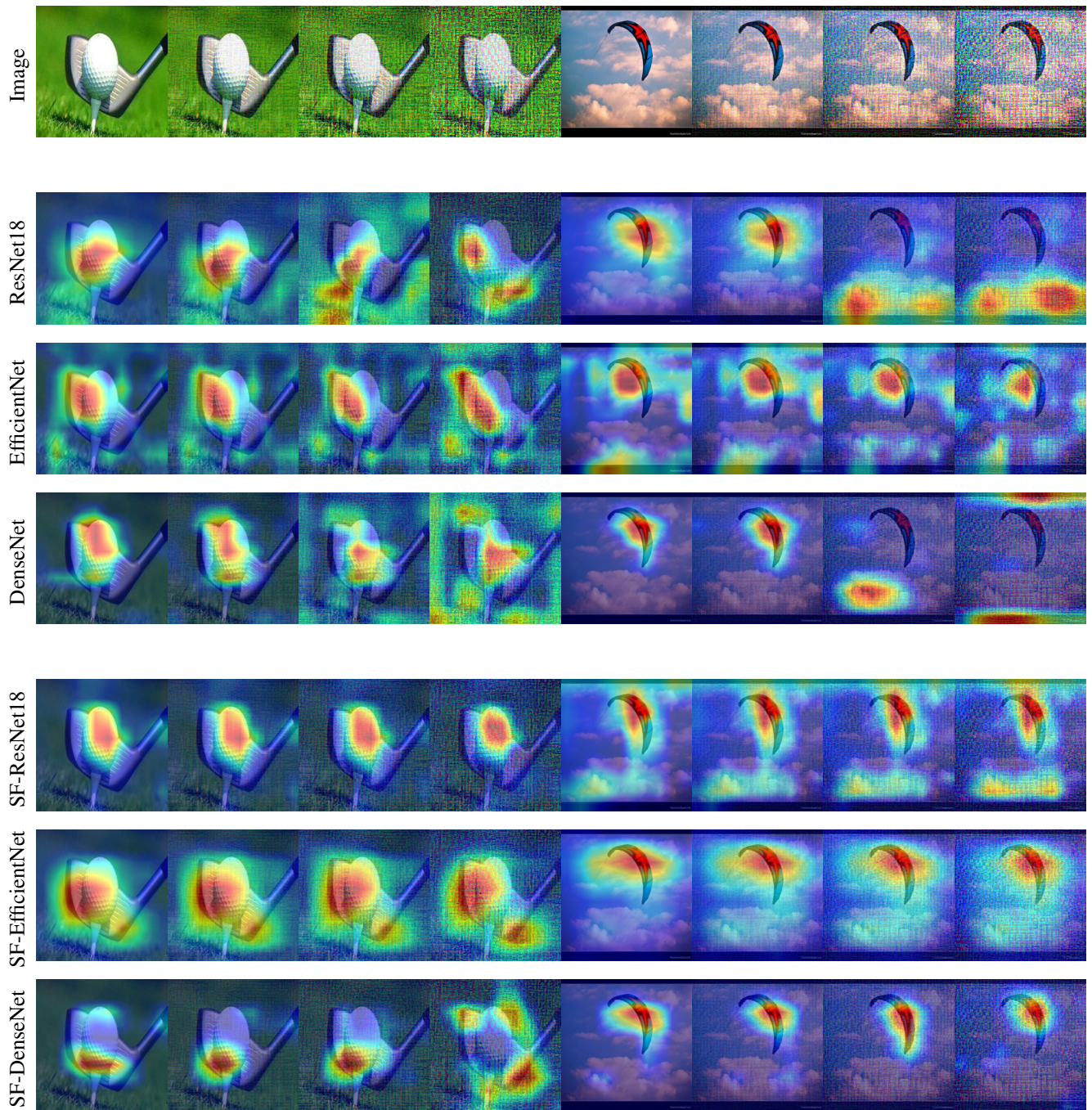


Figure 10: Grad-Cam visualizations of model attention on two adversarial examples generated from **SF-VGG11**. Each row shows the progression from $\epsilon = 0$ (not attacked) to $\epsilon = 0.1, 0.2$ and 0.3 from left to right.